

Angle-resolved-photoemission extended-fine-structure spectroscopy investigation of $c(2\times 2)$ S/Ni(011)

S. W. Robey, J. J. Barton, C. C. Bahr, G. Liu,* and D. A. Shirley

Materials and Molecular Research Division, Lawrence Berkeley Laboratory, University of California, Berkeley, California 94720 and Department of Physics and Department of Chemistry, University of California, Berkeley, California 94720

(Received 2 May 1986)

Measurements of the extended fine structure in the photoemission intensity from the S($1s$) core level were performed for a $c(2\times 2)$ overlayer of S on Ni(011). Four experimental geometries were employed, making this the most complete angle-resolved-photoemission extended-fine-structure (ARPEFS) study to date. Surface structural information was extracted from the ARPEFS using a combination of Fourier-transform techniques and comparisons to multiple-scattering calculations. The results of this analysis are in excellent agreement with previous studies of this system indicating that S adsorbs in a rectangular hollow site 2.20 ± 0.02 Å above a second-layer Ni atom. We further present evidence for a buckling of the second Ni layer, giving an expansion in the separation between the first Ni layer and the second-layer Ni atoms covered by S atoms of 11% from the bulk value, while second-layer Ni atoms not covered in the $c(2\times 2)$ structure assume essentially bulk positions. We also examine in detail the effects of multiple scattering on the extraction of this structural information from ARPEFS and present results for surfaces with S coverages greater than $\frac{1}{2}$ monolayer.

I. INTRODUCTION

Angle-resolved photoemission (ARP) is well known as a probe of surface electronic structure. An increasing number of studies have also used this technique to deduce surface atomic structure.¹⁻⁴ Surface structural information is contained in ARP due to final-state interference caused by scattering of the photoelectron from neighboring atoms.

Two experimental variants have been employed to measure these interference effects. Azimuthal photoelectron diffraction² is based on measuring the oscillatory structure in the photocurrent as the electron emission angle is scanned, while keeping the photon energy constant. An alternate method, used in this work, is variable-energy photoelectron diffraction. This technique consists of performing a constant-initial-state scan for a core level, with the electron emission direction held fixed. The measured photoelectron current oscillates as the photoelectron kinetic energy is varied. This is caused by interference between that part of the emitted photoelectron wave which travels directly to the detector and that part which propagates first to a neighboring atom, where it is elastically scattered toward the detector. The path-length difference for these two propagation paths leads to a phase difference at the detector. As the photoelectron kinetic energy is increased, this phase difference increases, resulting in a series of maxima and minima in the photoemission intensity. Originally this variable-energy method was called normal photoelectron diffraction.^{3,4} More recently, the same angle-resolved-photoemission extended fine structure¹ (ARPEFS) has been employed to better acknowledge the analogy to extended x-ray-absorption fine structure (EXAFS) and the advantages of non-normal emission directions.

Early studies of variable-energy photoelectron diffraction were successful in determining a number of surface structures.³ Extraction of structural information in these studies was implicit, in being based on comparisons of the data to low-energy electron-diffraction (LEED) -like multiple-scattering calculations.⁵ The attractiveness of ARPEFS was recently enhanced by a study which indicate that Fourier transforms could be employed to facilitate explicit data analysis, yielding more direct access to structural information.¹ That study, along with the presentation of a theoretical model based on a more EXAFS-like cluster approach⁶ to describe the scattering, led to the name ARPEFS.

In this paper we report ARPEFS experiments based on photoemission from the S($1s$) level in the system $c(2\times 2)$ S/Ni(011). This research was motivated by several goals. First, the $c(2\times 2)$ S/Ni(011) was chosen in part because it has been well studied in previous LEED (Refs. 7 and 8) and ion-scattering⁹ experiments. This system therefore provides a stringent test for ARPEFS to generate a unique, accurate, and correct surface structure. In this context, for example, the ion-scattering analysis indicated an expansion of the first Ni interplanar separation by 6%. To be competitive, ARPEFS would have to confirm this result.

The analysis of the ARPEFS $\chi(k)$ curve (defined below) can be performed at three levels of increasing sophistication. Two of these are analogous to standard EXAFS analyses. The first is based simply on Fourier transforming $\chi(k)$ to form a spectrum $F(r)$ with intensities at various "path-length differences." These distances can then be compared with expectations based on trial geometries. The second, more quantitative, level consists of selecting a peak in $F(r)$ that arises mostly from one path-length difference, if one is available, and back-

transforming to derive the value for that distance. At the third level, the ARPEFS curve is fitted with a theoretical curve for which structural parameters are thereby optimized. Our second goal in analyzing the $c(2 \times 2)\text{S}/\text{Ni}(011)$ data is to ascertain the extent and validity with which structural information can be obtained from each level of analysis. Until now this question has been uncertain and even controversial, for lack of adequate data.

Finally, previous ARPEFS studies^{1,10} have concentrated on data taken for high symmetry crystallographic directions. However, there is no reason to expect that the adsorption site will maintain the bulk symmetries, especially when considering more complicated systems. This study has attempted to select experimental geometries which help elucidate the surface structure¹¹ and test the sensitivity of the ARPEFS to moderate angle changes.

The remainder of this paper is organized as follows. Section II describes experimental details and provides a brief description of the reduction of the raw data to the $\chi(k)$ form. It concludes with the presentation of $\chi(k)$ curves for the $c(2 \times 2)\text{S}/\text{Ni}(011)$ system collected for several experimental geometries. In Sec. III we present a discussion of the theoretical aspects of ARPEFS. Section IV discusses the analysis of the data, first using Fourier-transform methods, followed by an r -factor analysis performed using comparisons to multiple-scattering calculations. In Sec. V we present some results obtained for the $\text{S}/\text{Ni}(011)$ system at greater than $\frac{1}{2}$ monolayer (ML) coverage. A summary and conclusions are given in Sec. VI.

II. EXPERIMENTAL DETAILS

A. Equipment

These experiments were performed using synchrotron radiation from Beamline III-3 located at the Stanford Synchrotron Radiation Laboratory, on the SPEAR (Stanford Positron-Electron Accelerator Ring) storage ring. This soft x-ray beam line is equipped with a UHV double-crystal monochromator described in detail elsewhere.¹² For this work, involving photoemission from the $\text{S}(1s)$ core level (binding energy equal to 2472 eV), a pair of $\text{Ge}(111)$ crystals were used to produce monochromatic x rays in the spectral range from 2500 to 3000 eV. The photon-energy resolution provided by the monochromator was approximately 2 eV through this range. The synchrotron radiation is $\geq 98\%$ linearly polarized.

The UHV experimental chamber was described in detail in previous work.¹³ It consists of two levels of instrumentation. The upper level is used for sample preparation and characterization. It contains a four-grid LEED system employed for both LEED and Auger measurements, along with an ion gun for sample cleaning and a gas inlet system for preparing adsorbed overlayers. The lower level contains the hemispherical electrostatic analyzer employed for collecting angle-resolved photoelectron spectra. This analyzer is mounted on a carriage which allows rotations under UHV conditions of 360° about a vertical axis and 100° about a horizontal axis. The analyzer was operated with a constant pass energy, giving an analyzer

contribution to the resolution of ~ 1 eV. The angular resolution of the input optics was $\pm 3^\circ$.

B. Sample preparation

The $\text{Ni}(011)$ crystal was cut ($7 \times 7 \times 1$ mm³) from high-purity (99.999%) single-crystal stock, and mechanically polished to within $\pm 1^\circ$ of a (011) orientation as determined by Laue backscattering. It was then chemically etched¹⁴ before mounting on a high-precision sample manipulator for insertion in the experimental chamber. The manipulator allowed linear motion along three perpendicular axes and rotations about both an axis in the crystal surface and about the crystal normal. Sample heating was accomplished by electron bombardment from a tungsten filament located behind the Ta sample plate on which the Ni crystal was mounted. Temperatures were measured using an infrared pyrometer.

After installation in the experimental chamber, which maintained a typical pressure of 2×10^{-10} Torr, the crystal was cleaned by repeated cycles of argon-ion etching and annealing to 800°C . This procedure was sufficient to remove all impurities except carbon. The carbon was then removed by heating the crystal to 700°C after exposure to 1×10^{-8} Torr of O_2 for several minutes. Auger electron measurements were performed using the four-grid LEED optics in the retarding field mode. These measurements showed no detectable traces of carbon, oxygen, or sulfur. The $c(2 \times 2)$ overlayers of sulfur were formed by ambient exposure of 1.5–2 L [where L denotes langmuirs ($1 \text{ L} = 10^{-6}$ Torr sec)] of H_2S , followed by annealing to 150°C . Auger measurements for the $c(2 \times 2)$ structure showed no trace of impurities other than sulfur. The ratio of the $\text{S}(152 \text{ eV})$ Auger intensity to that of $\text{Ni}(61 \text{ eV})$ was reproducible for the several overlayers prepared for the ARPEFS measurements.

C. Geometries

ARPEFS measurements were performed for several different experimental geometries. The emission and photon polarization angles for each geometry were determined by He-Ne laser autocollimation through the experimental chamber viewports. The angles determined in this manner have an estimated accuracy of $\pm 2^\circ$.

The experimental geometries employed in performing the ARPEFS measurements, described below, are illustrated in Fig. 1. This figure depicts a section of the [011] Ni surface, indicating the photoelectron emission angles for which ARPEFS data were collected. We include the S atoms in the rectangular hollow site. This will be shown to be the correct adsorption site in the analysis below, in agreement with previous studies.^{7–9} The geometries are as follows.

(a) Emission along the surface normal. The photon polarization vector was directed 40° from the surface normal toward [100].

(b) Photoelectron emission 38° from the surface normal toward [100] with the polarization 78° from the normal toward [100].

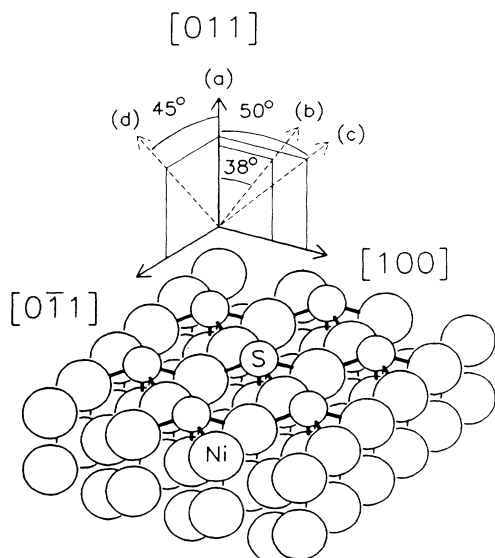


FIG. 1. View of the Ni(011) surface with a $c(2 \times 2)$ S overlayer, indicating principal crystallographic directions and the photoelectron emission directions for which ARPEFS data were collected.

(c) Emission 50° from the surface normal toward [100]. The polarization vector was in the surface along [100].

(d) Emission along [001]. The polarization was 75° from the surface toward [011].

The normal emission data primarily contains information about atoms below the adsorbed sulfur atom. Geometries (b), (c), and (d) were chosen to increase the sensitivity of the measurements to atoms on either side of the S atom, particularly near-neighbor Ni atoms. Geometry (d) was also chosen for comparison with previous data on the Ni(001) surface.¹ For geometries (b) and (c), the azimuthal angle was $\sim 3^\circ$ from [100] due to limitations of the sample motion.

D. Data collection and reduction

For each geometry a series of photoelectron spectra at different kinetic energies were collected using an energy window which included the S(1s) core level. The reduction of these data then requires extracting the intensity in the core peak and normalizing for the photon flux. This normalization is important primarily for removing sharp changes such as those due to monochromator crystal "glitches" or new fills of the SPEAR storage ring. The resulting intensity as a function of the photoelectron kinetic energy is, in analogy with EXAFS, composed of a slowly varying, atomiclike portion and a rapidly oscillating contribution due to the interference effects of electron scattering from neighboring ion cores. The total measured intensity can be written

$$I(E) = [\chi(E) + 1]I_0(E). \quad (1)$$

Here $I(E)$ represents the total intensity as a function of the photoelectron kinetic energy E , $\chi(E)$ is the oscillatory interference function, and $I_0(E)$ is a slowly varying function.

$I_0(E)$ can contain contributions from several sources. In the simplest approximation, $I_0(E)$ arises from the energy dependence of the photoexcitation matrix element. However, $I_0(E)$ can also contain slowly varying structure introduced by data collection or reduction procedures, as well as components of ARPEFS with small scattering path lengths. Because the exact form of this function is unknown, the low-frequency structure is extracted by fitting the data with a quadratic or cubic polynomial or a smooth cubic spline. The unavoidable shortcoming of this procedure is that real ARPEFS structure with scattering path lengths less than ~ 1.5 Å can be unintentionally distorted or completely removed.

With $I_0(E)$ determined as outlined above, $\chi(E)$ can then be formed as

$$\chi(E) = [I(E)/I_0(E)] - 1. \quad (2)$$

Further details of this data reduction process can be found elsewhere.¹⁵

For Fourier-transform data analysis, it is necessary to convert $\chi(E)$ to $\chi(k)$. The photoelectron kinetic energy E measured outside the solid is related to the wave number of the photoelectron inside the solid by

$$k = (1/\hbar)[2m_e(E + V_0)]^{1/2}, \quad (3)$$

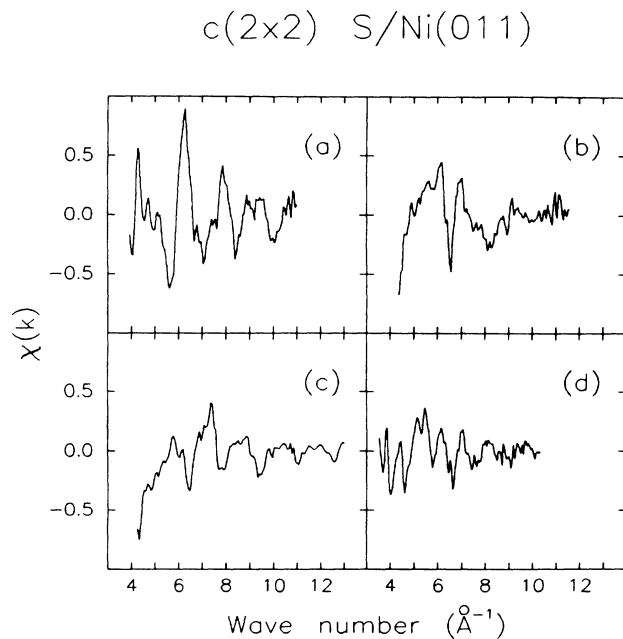


FIG. 2. ARPEFS data in $\chi(k)$ form for the experimental geometries indicated in Fig. 1 and described in the text. (a)–(d) correspond to the respectively labeled directions in Fig. 1.

where m_e is the electron mass and V_0 is the inner potential of the solid. The value of V_0 is typically about 10 eV, but the exact value is unknown and is slightly energy dependent. The inner potential is therefore treated as an adjustable parameter in the Fourier-transform analysis. The $\chi(k)$ curves for each of the geometries indicated in Fig. 1 are presented in Fig. 2. An inner potential of 10 eV was assumed for these curves.

III. THEORETICAL DISCUSSION

Theoretical treatments of ARPEFS, or photoelectron diffraction, have been presented by several groups.^{5,6,16-18} The degree of sophistication has varied from simple single-scattering cluster models to fully dynamical treatments derived from LEED theory. Recent work by Barton *et al.*^{18,19} provided a bridge between these two extremes. That work included important multiple-scattering and spherical wave effects, while retaining the physical insight offered by a cluster approach. This section will be devoted to presenting a qualitative discussion of the major theoretical aspect of ARPEFS.

A. Single scattering

Because we are concerned primarily with presenting the most important qualitative ideas that can be extracted from detailed theories of ARPEFS, we will begin by presenting an expression for $\chi(k)$ which is derived with some simplifying assumptions. These involve representing the photoelectron wave at the scattering center using the plane-wave approximation^{20(a)} and including only single scattering. After considering the implications of this simple model, we will discuss the modifications that must be considered when the dominant effects of multiple scattering are included.

Using these simplifications and assuming photoemission from an initial state with s symmetry, the expression for $\chi(k)$ can be written,

$$\chi(k) = 2 \sum_j \frac{\cos\beta_j}{\cos\gamma} \frac{|f(\theta_j)|}{r_j} \cos[k(r_j - r_j \cos\theta_j) + \phi_j] \times e^{-\Delta R_j/\lambda} e^{-\sigma_j^2(1-\cos\theta_j)k^2}. \quad (4)$$

The summation is over all atoms near the adsorbed "source" atom from which the core-level photoemission is being measured. The angle β_j is measured between the photon polarization vector and the vector connecting the emitting and scattering atoms, r_j is the bond length between the emitting and j th scattering atoms, and γ is the angle between the polarization and the electron emission direction. The j th scattering atom is characterized by a complex scattering amplitude,

$$f(\theta_j) = |f(\theta_j)| e^{i\phi_j}.$$

Both the magnitude of $f(\theta_j)$ and the phase ϕ_j depend on the scattering angle θ_j and the photoelectron wave number, k . The emission angle-dependent path-length difference is given by $\Delta R_j = r_j - r_j \cos\theta_j$. Inelastic damping due

to thermal vibrations is included using a Debye-Waller term, where σ_j^2 is the mean-square relative displacement between the emitting and scattering atoms, projected on the photoelectron momentum change direction. Inelastic losses due to excitation of plasmons and electron-hole pairs by the energetic photoelectron are incorporated in an electron mean-field path λ .

Each term in this expression represents the ARPEFS due to interference between the direct wave and the wave scattered from a neighboring ion core potential, as described previously. The cosinusoidal factor has a frequency given by the path-length difference for that scattering event, with an additional small contribution to the phase from the complex scattering amplitude. These oscillatory functions are multiplied by angle- and energy- (or wave-number-) dependent amplitudes. The amplitudes for given scattering atoms are determined by a number of factors^{6,10}

(1) The finite electron mean free path, the lower correlation of thermal vibration at larger distance, and the $1/r_j$ dependence of the oscillation amplitude all act to limit strongly the number of atoms which contribute significantly to the ARPEFS. Thus the ARPEFS is dominated by the local atomic structure.

(2) The scattering amplitude $|f(\theta_j)|$ is peaked in the forward and backscattering directions, with only weak scattering for angles in between. Thus, atoms which provide near backscattering will usually produce large intensity modulations in $\chi(k)$. Structure at low ΔR_j values due to near-forward scattering will become important for near-grazing emission or for subsurface adsorption.

(3) The factor $\cos\beta_j$ arises from the orientation of the photon polarization with respect to the vector from the emitting atom to the scattering atom. This factor determines the amplitude of the photoelectron p wave that is incident on the scattering center. Orientation of the polarization such that the bond vector for a particular scattering atom lies in the nodal plane of the p -wave final state will lead to negligible intensity for that scattering path length.

Two major conclusions can be drawn from this discussion. First, scattering involving near neighbors and near backscattering will produce strong ARPEFS modulations. Secondly, specific atoms can be enhanced relative to others by proper choice of the photon polarization direction. This discussion, however, has not considered the effects of multiple scattering. Previous studies have indicated that the single-scattering treatment is not adequate. Comparisons by Tong *et al.*⁵ of fully dynamical calculations to kinematic theory indicated that the single-scattering model is inadequate for a quantitative description of ARPEFS. Other recent studies^{18,21} also indicated that multiple scattering is important in many cases.

B. Multiple scattering

Because of the strong peaking of the scattering amplitude in the forward direction, the dominant multiple-scattering events will be those which include forward scattering. The quasidynamical theory²² of Tong *et al.*, which included all single-scattering events and all orders

of forward multiple scattering, gave curves essentially identical to their fully dynamical theory for photoelectron energies above 100 eV.⁵ Since additional near-forward scattering events will introduce practically no extra path-length difference, the inclusion of multiple scattering will serve primarily to enhance the amplitude of a single-scattering event when that event is preceded or followed by forward scattering. The additional forward-scattering events act to focus the electron amplitude along the forward direction. Since backscattering will always be followed by a subsequent forward scattering through the emitting atom, the inclusion multiple scattering will serve to enhance backscattering events even more strongly than is predicted for a single-scattering theory.

In addition to this modification of the single-scattering amplitude, there will also be contributions to the scattering phase shift for each additional forward-scattering event. A correct determination of the amplitude enhancement and forward-scattering phase shift requires the consideration of the plane-wave approximation. The study of Ref. 19 indicates that correct treatment of spherical wave effects is necessary for near-forward scattering. Thus the correct inclusion of the dominant multiple-scattering effects requires a treatment which goes beyond the plane-wave approximation. Attempts to treat multiple scattering within the plane-wave approximation give results which are nearly as inaccurate as those introduced by completely neglecting the multiple scattering.

IV. DATA ANALYSIS

The most general method of analysis that can be employed to extract structural information from ARPEFS data involves applying procedures similar to those employed in LEED studies. The data are compared to calculations using an “*r* factor” as a quantitative measure of the level of agreement. The results of such an analysis using comparisons to multiple-scattering calculations will be presented in Sec. IV B. However, consideration of the form of Eq. (1) compared to the analogous expression describing EXAFS (Ref. 20) presents the possibility of using Fourier-transform techniques. This approach was suggested in the work of Lee,¹⁷ and later an exploratory study of this applicability was performed by Hussain *et al.*,²³ using theoretical simulations of ARPEFS data to obtain an adequately long data range.

The application of Fourier-transform techniques to extended data range ARPEFS data was first performed for $c(2 \times 2)\text{S}/\text{Ni}(001)$.¹ This work indicated that Fourier-transform techniques can yield useful information. We shall examine the extent to which this relatively simple, direct analysis can provide information about the adsorption geometry of $c(2 \times 2)\text{S}/\text{Ni}(011)$. We will also investigate the effects of multiple scattering on the extraction of this information.

A. Fourier-transform analysis

This subsection will be further divided into three parts. First we present a qualitative discussion of the Fourier transforms of ARPEFS data for $c(2 \times 2)\text{S}/\text{Ni}(011)$ based

on the ideas presented in Sec. III. This will be followed by a quantitative analysis employing the filtering and backtransform procedures developed for the treatment of EXAFS data.²⁴ Finally, we will illustrate the effects of multiple scattering that are evident in these data.

1. Qualitative discussion

Considering the form of $\chi(k)$ given in Eq. (1), and the above analogy with EXAFS, one would expect peaks to appear in the Fourier transform of this function at positions given by the path-length difference, $\Delta R_j = r_j(1 - \cos\theta_j)$, for scattering from neighboring atoms. For a given scattering atom, this path-length difference changes with the electron emission angle, leading to different structure in the Fourier transform for each different emission angle. Thus, data taken at several emission angles should allow one to establish the adsorption site through examination of the Fourier transforms, provided that they can be interpreted in a reasonably simple manner.

The positions of peaks in the Fourier transform will differ slightly from the value of ΔR_j , due to the additional scattering phase shift ϕ_j . However, this phase shift is nearly independent of k , with only a small linear contribution leading to small shifts. Large shifts in ΔR_j can occur when there is strong structure in the phase shift, as happens when the scattering angle approaches a value for which there is a zero in the scattering amplitude—the generalized Ramsauer-Townsend resonance.²¹ This complication must be studied independently by considering the angle and energy dependence of the appropriate complex scattering amplitude.

We now turn to an examination of the S/Ni(011) data. Fourier transforms of the normal emission, the 38°, and the 50° data are presented in Fig. 3. The discussion which

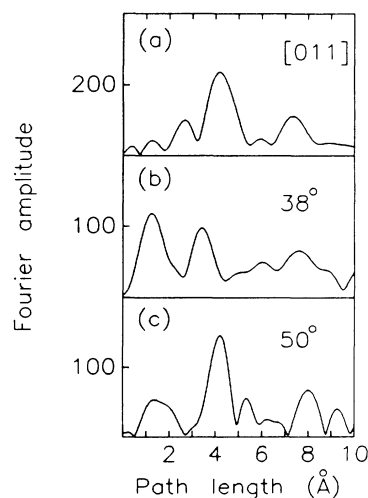


FIG. 3. Fourier transforms of the $\chi(k)$ data given in Fig. 2 for geometries (a), (b), and (c). A Gaussian-broadened (1 Å) window function was used to reduce truncation effects. Note the change in scale for the lower two panels.

follows will concentrate on the dominant features in each transform.

The normal emission transform is dominated by a strong peak at 4.2 Å with smaller structure at approximately 3 and 7.5 Å. The data set taken with an emission angle of 50° shows a strong peak at 4.1 Å, though this peak is significantly weaker than the 4.2-Å peak in the normal emission (the 50° transform is scaled by a factor of 2). This geometry also gives structure in the 1–2 Å range and at 8 Å. Data taken with an emission angle of 38° yield two dominant peaks, at ~1.2 and 3.7 Å.

Inspection of these Fourier transforms, coupled with the ideas presented in Sec. III, and consideration of the plausible adsorption sites for S on the Ni(011) surface—atop on the first layer, short bridge, long bridge, or rectangular hollow—leads to the conclusion that adsorption occurs in the rectangular hollow. The atoms giving dominant contributions to the structure described above can be identified with reference to Fig. 4. The very strong 4.2-Å peak in the normal emission data is due to backscattering from the second-layer Ni atom labeled (2) in Fig. 4. The intensity in this backscattering peak is considerably enhanced due to forward scattering through the sulfur atom. The 4.1-Å peak in the 50° data is dominated by two symmetrically equivalent atoms in the first Ni layer which have scattering angles of ~144°, close enough to backscattering to maintain a reasonably large scattering amplitude. These atoms are labeled (1) in Fig. 4. The peak at 3.7 Å in the 38° data is also due almost exclusively to these same atoms. The reduction in intensity of the 38° peak relative to that in the 50° case is consistent with a decrease in the scattering amplitude in going from 144° scattering for the 50° geometry to 137° scattering for the 38° data.

Additionally, the structure of 3 Å in the normal emission data strongly supports adsorption in the rectangular hollow. The other sites do not provide an explanation for this peak, which has a shorter path-length difference than the dominant 4.2-Å peak at normal emission. For the rectangular hollow this structure is easily explained in terms

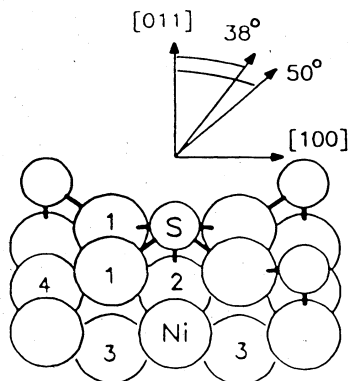


FIG. 4. This figure displays the cluster of atoms around the adsorbed S atom which provide the dominant structure in the ARPEFS data. For an explanation, see the text.

of scattering from the four near-neighbor Ni atoms in the first layer. Thus, by examination of the Fourier transforms, we find convincing evidence that the S adsorption site is the rectangular hollow, in agreement with the previous ion scattering and LEED experiments. The Fourier-transform structure is inconsistent with other possible adsorption sites. Although other sites could provide explanations of the structure for one experimental geometry, a combination of two data sets (in particular the normal emission and 50° data) favors the rectangular hollow site.

2. Filter and backtransform analysis

Having identified the adsorption site, and thus the particular atoms contributing to the dominant peaks in the Fourier transform for each geometry, more precise quantitative information can be obtained by employing the filtering and backtransform analysis procedures developed for EXAFS data.²⁵ The analysis consists of windowing the Fourier peak of interest, backtransforming this peak, and extracting the experimental phase function. The total phase function ϕ_T is given by the argument of the cosine in Eq. (1),

$$\phi_T = kr_j(1 - \cos\theta_j) + \phi_j. \quad (5)$$

If the appropriate theoretical scattering phase shift ϕ_j is removed, the remaining function is linear in k with a slope given by $\Delta R_j = r_j(1 - \cos\theta_j)$, the desired path-length difference. A complication exists due to the unknown value of V_0 , the inner potential. The inner potential is therefore treated as an adjustable parameter which is varied until the most linear function, $kr_j(1 - \cos\theta_j)$, is obtained.

The results of this analysis performed on the 4.2-Å peak in the normal emission data, the 3.7-Å peak in the 38° data, and the 4.1-Å peak in the 50° data are presented in Table I. These structures were chosen because they can be assigned primarily to single or symmetrically equivalent atoms, so that a single path-length difference can be extracted in each case. The other large peak in the 38° data at ~1.2 Å is not treated because this structure cannot be easily identified with a single-scattering path length. Also, structure in this low path-length region can be strongly influenced by the data reduction procedures as discussed in Sec. II.

TABLE I. Path length values (in Å) obtained from the dominant peaks in the normal emission (0°), 38°, and 50° Fourier transforms, using the analysis discussed in the text. Note that the analysis consistently produced values of V_0 within 1 eV of each other.

Expt. geometry	ΔR	V_0 (eV)
0°	4.36(4)	10
38°	4.02(5)	9
50°	4.18(4)	9

The path length given by

$$\Delta R_j = 4.36 \text{ \AA} = r_j(1 - \cos\theta_j), \quad \theta_j = \pi \quad (6)$$

for the normal emission data indicates a bond length of 2.18 Å between the S and the Ni atom in the second layer directly below. The data taken off-normal deserve some comment due to the $\sim 3^\circ$ azimuthal rotation from the plane containing [100]. The major effect of this misalignment will be to produce two slightly different scattering paths, instead of two symmetrically identical paths, contributing to the dominant peak at 4.1 Å. However, the small difference between these two paths is well beyond the resolution of the measurement. Since the change in the scattering phase shift and amplitude for the two different scattering angles is small, the analysis produces a value of the path length which is the average of the two values and, within the accuracy of the experiment, is equivalent to the value that would be obtained with no azimuthal rotation. With this in mind, the value of 4.18 Å for the path-length difference in the 50° data indicates a bond length between the S atom and the near-neighbor atoms in the first Ni layer of 2.31 Å. Alternatively, this is equivalent to specifying a value of 0.82 Å for d_1 , the height of the sulfur atom above the first nickel layer.

The value extracted for the weaker 3.7-Å peak in the 38° data, corresponding to scattering from the same set of two atoms as for the 50° case, is 4.02 Å. The larger shift of the peak in the Fourier transform from the backtransformed value, compared to the previous two cases, is partially due to the previously mentioned generalized Ramsauer-Townsend effect. The $\sim 137^\circ$ scattering angle for the structure in the 38° data is close enough to a zero in the Ni scattering amplitude at 129° to produce a larger shift. However, the path-length value obtained from the backtransform analysis is in good agreement with the value of 4.00 Å that is predicted based on the 2.31-Å bond length determined from the 50° data. Considering the smaller amplitude of the structure in the 38° data, the results of the backtransform analyses show very good consistency between the two independent measurements. The errors indicated in Table I, and also in Table II below, are based on the precision of the procedure and estimations of the effects of errors in the theoretical phase shifts and errors in experimental angles.

With the bond lengths of the S atom to its near neighbors in the first and second Ni layers known, the details of the adsorption site can now be determined. As stated, the 2.31-Å bond length to the first-layer Ni atoms indicates a value of $d_1 = 0.82$ Å. This value, in conjunction with the value of 2.18 Å for the S-second-layer-Ni separation, then provides a value of 1.36 Å for the interplanar separation between the first and second Ni layers. This represents an expansion of this separation by 9% from its bulk value of 1.245 Å. Table II summarizes the results of this analysis and also presents the results of the previous ion scattering experiment for comparison. In this table, S-Ni₁ and S-Ni₂ represent the bond lengths to atoms (1) and (2) in Fig. 4, respectively. The parameter d_{12} is the interplanar separation between the first and second Ni layers and Δ (%) is the percent change in this spacing from the bulk value.

TABLE II. Structural parameters (in Å) determined from the path-length values presented in Table I. A description of the parameters presented is provided in the text. The results of the ion scattering experiment performed by Van der Veen *et al.* in Ref. 9 are included for comparison.

Parameter	ARPEFS	Ion scattering
S-Ni ₁	2.31(3)	2.32
S-Ni ₂	2.18(2)	2.18
d_1	0.82(7)	0.87(3)
d_{12}	1.36(7)	1.31(4)
Δ (%)	+ 9(6)	+ 6(3)

The excellent agreement of the backtransform analysis with the ion scattering experiment supports the previous assignments of the dominant structure in the Fourier transforms. This also supports the idea that the structure in the Fourier-transformed data for an unknown system can be interpreted in a reasonably simpler manner, thus aiding in determining the adsorption site and, in favorable cases, allowing the extraction of bond lengths. The ability to use this attractive feature of the ARPEFS technique does, however, require careful consideration of the possible adsorption geometries so that the experiment can be devised to make best use of the strong modulation which will normally occur for near-backscattering geometries. For instance, although the Fourier transform of the 38° data provides information that is helpful in determining the adsorption site, the stronger structure in the 50° data is clearly preferable.

3. Multiple-scattering effects

Before turning to an r -factor analysis of the data, we will discuss the effects of multiple scattering displayed in this data. As noted previously, the backtransform analysis requires the removal of the scattering phase shift ϕ_j . As in the case of the scattering amplitude, the phase shift also requires the consideration of multiple scattering. In addition to enhancing the intensity of a single scattering, forward-scattering events will also add contributions to ϕ_j . This affects primarily the normal emission data—the backscattered wave from the second-layer Ni atom must necessarily be forward scattered through the S atom as it propagates to the detector. The backtransform analysis of the normal emission data has accounted for this effect by employing a double-scattering phase shift. An attempt to analyze these data using only the single backscattering phase shift $\phi(\pi)$ leads to a path-length value of 4.40 Å instead of 4.36 Å, but more importantly, it also requires a nonphysical value of $V_0 \approx 30$ eV fit the data. Thus a single-scattering model attempts to compensate for the approximately constant additional phase shift due to double scattering by variation of the V_0 parameter outside an acceptable range.

We further illustrate this effect in Fig. 5. The large-dot curves in Figs. 5(a) and 5(b) represent the filtered and backtransformed data for the dominant peaks in the 50° and normal transforms, respectively. The solid curve in

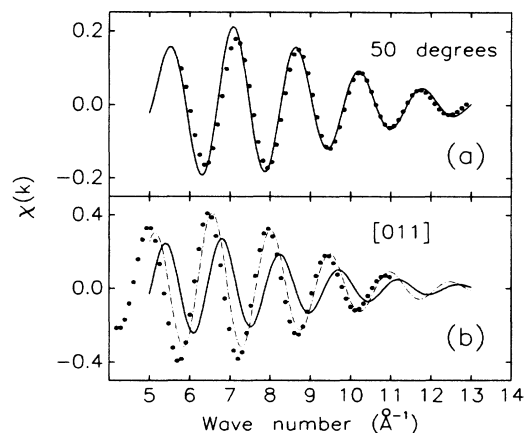


FIG. 5. Theoretical simulations of filtered data for the 50° emission data and the [011], or normal emission, data. The dotted curves are the data filtered to include only the strongest peak in the Fourier transform for each respective geometry. The solid lines are simulations employing a single-scattering theory, and the dashed-dotted line is the result of a calculation including double scattering.

Fig. 5(a) shows a theoretical simulation of the backtransformed 4.1-Å peak in the 50° data. As stated, this peak should be well described with single scattering. The solid curve was calculated using a single-scattering model,

$$\chi(k) = 2Ne^{-\Delta R_j/\lambda} e^{-\sigma_j^2 k^2 (1 - \cos\theta_j)} \times \cos[kr_j(1 - \cos\theta_j) + \phi_j]. \quad (7)$$

The value of λ , the electron mean free path, was obtained from the values of Seah and Dench²⁵ and σ_j^2 , the appropriate mean-squared relative displacement due to thermal vibrations, was then determined by the best fit to the backtransformed data. The value of σ_j^2 thus obtained was 0.009 Å². The values of the number of contributing atoms, $N=2$, and the path-length difference, $\Delta R_j=4.18$ Å, are known. The important point is that reasonable values of the parameters λ and σ_j yield a good simulation of the backtransformed data, as shown in Fig. 5(a).

Considering now the normal emission data in Fig. 5(b), we expect that with λ and σ_j taking values close to those which provided a good simulation of the 50° data we should obtain a qualitatively similar simulation for this data. The fact that the scattering events contributing to the 4.1-Å peak in the 50° data are in the surface layer while the scattering atom which dominates the normal emission peak at 4.2 Å is in the second layer would be expected to lead to somewhat different values for the thermal vibrations. However, both cases involve atoms which are near neighbors so that the difference should not be large. The result, assuming only single scattering, is presented as the solid line in Fig. 5(b). It can be seen that the data show a much larger amplitude and there is also a large, approximately constant, phase shift. The same V_0 value was used to convert the photoelectron kinetic energy

to wave number k in both the normal emission and the 50°, case, $V_0=9$ eV. Correction of the remaining large phase shift error requires a value of $V_0 \approx 30$ eV if the single-scattering model is forced to fit the data.

The dotted-dashed line in Fig. 5(b) presents the result of the same simulation, but including the effect of the additional multiple scattering through the intervening S atom. This simulation also included an exact treatment of the spherical wave scattering. The agreement is much better in this case and nearly as good as that provided by the 50° example. It is clear from the magnitude of these effects that multiple-scattering effects must be included if quantitative interpretations of ARPEFS are sought.

B. Multiple-scattering calculations

The Fourier-transform analysis presented in the preceding section concentrated primarily on only the dominant structure in the transforms. There is also weaker structure in the transforms which indicates that the ARPEFS contains additional structural information. An alternative approach to the analysis consists of direct comparison of the $\chi(E)$ curves to theoretical curves calculated assuming a specific adsorption geometry, in a manner analogous to the treatment of LEED data. This method provides a straightforward method of testing the data for additional, less dominant structural parameters. Even here, however, the ability to interpret the Fourier transforms in a relatively simple manner provides a useful guide in assessing to which structural variables an experimental geometry will be most sensitive.

In this section we present the results of such an analysis based on comparisons to multiple-scattering, cluster calculations. These calculations are described in detail elsewhere.¹⁸ A brief outline of the major features will be presented here.

As discussed above, a quantitative theory of ARPEFS requires the inclusion of important multiple-scattering and spherical wave effects. The cluster calculations performed in this work have included multiple scattering to fourth order as well as the dominant corrections to the plane-wave approximation due to the spherical nature of the photoelectron wave using the approximations presented by Barton *et al.*¹⁹ The finite mean free path was treated as an exponential damping factor, $e^{-r/\lambda}$, with $\lambda = ck$. The value of c was determined by fitting to the values given by Seah and Dench²⁵ for Ni, giving $c=0.78$. Thermal effects were treated using a correlated Debye model which accounted for increased thermal vibrations near the surface and anisotropies in different crystallographic directions.¹⁸ The inputs in this model were determined using theoretical calculations of the mean-square displacements for the Ni(011) surface²⁶ as a guide. The bulk Debye temperature Θ_D^b was taken as 390 K, and the Ni surface Debye temperatures were set at 270, 270, and 310 K for the [110], [100], and [1 $\bar{1}$ 0] directions respectively. The Debye temperatures for the sulfur overlayer were assumed to be given by the Ni surface values appropriately adjusted for the difference in masses, giving 365, 365, and 420 K for the [110], [100], and [1 $\bar{1}$ 0] directions, respectively. The theoretical curves were only

weakly dependent on the choice of these parameters. The $\pm 3^\circ$ angular resolution of the experiment was included as described in Ref. 18. The effect of the inner potential was included as an energy-independent shift of the kinetic energy scale.

The phase shifts used in these calculations were computed using a modified version of the program developed by Pendry for LEED.²⁷ The Ni potential was obtained from the self-consistent local-density-approximation (LDA) calculations of Moruzzi *et al.*²⁸ The S phase shifts were calculated using a potential obtained from atomic Hartree-Fock wave functions. The wave functions were truncated and renormalized at a muffin-tin value $R_{\max} = 1.05$ Å. Various values of R_{\max} were tested and produced no strong differences in the results of the analysis. The exchange potential was calculated using an $X\alpha$ approach with α taken from the work of Schwarz.²⁹ A total of 16 phase shifts were calculated for each potential for energies up to 500 eV.

The first step in the analysis consists of smoothing the data by filtering at 10 Å. Calculations were then performed including a cluster size large enough to include all path lengths with values ≤ 10 Å. For the off-normal geometries, the low path-length structure less than 2 Å was filtered due to uncertainties in measuring this structure. The calculations were then performed using these same low path-length cutoffs.

For the present analysis, a simple r factor was chosen. It consists of forming

$$r = \int [I_e(E) - I_t(E)]^2 dE / \int I(E)^2 dE. \quad (8)$$

Here $I_e(E)$ is the intensity of the experimental curve as a function of the energy and $I_t(E)$ is the intensity of the theory. The analysis proceeded by assuming an adsorption geometry and performing the multiple-scattering calculation. The level of agreement between the theory and experiment was evaluated by calculating r . The geometry was varied until a minimum in r was located. For each geometry comparisons were made to calculated curves with V_0 values of 8, 10, and 12 eV. The r factors determined in this manner were then averaged to give a final r value. This r factor is simple by present-day LEED standards,³⁰ but nonetheless provided consistent results for the values of parameters obtained from different experimental curves. Due to the $\pm 2^\circ$ – 3° accuracy with which experimental geometries are determined, the emission angle was varied to obtain the best simulation of the experimental curves. The angles obtained were within 3° of the nominal value in all cases. The final structural parameters determined by the r -factor analysis were only slightly (~ 0.02 Å) dependent on the angle used, except for the determination of d_1 from the [001] data. For this geometry, there are several Ni near neighbors which have scattering angles of $\sim 129^\circ$ —two atoms in the first Ni layer and the Ni atom directly below the S atom. This angle is very close to the scattering for which the generalized Ramsauer-Townsend resonance is observed in Ni.²¹ The scattering amplitudes and phases of these atoms thus depend strongly on the scattering angle, or equivalently, the emission angle. The minimum in the r factor was found to shift by 0.07 Å for angle changes of 3° . However, the value of

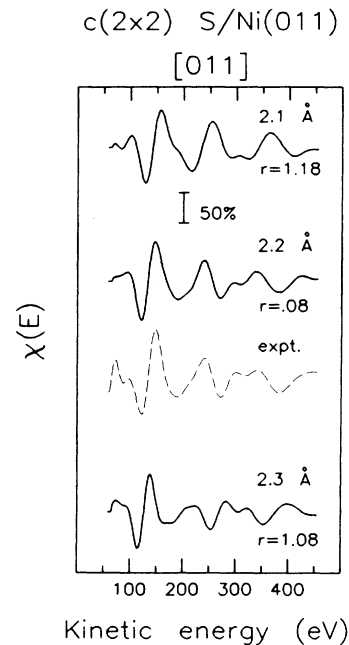


FIG. 6. Comparison of the normal emission data to multiple-scattering calculations for several values of the S-to-second-layer-Ni distance, indicating the sensitivity of the normal emission geometry to this parameter.

$d_1 = 0.81$ Å presented below for an emission angle of 45° had an r -factor minimum that was slightly lower than those found for other angles.

In Fig. 6 we present a comparison of the filtered normal emission data to calculations performed for several different values of S-Ni₂. The strong dependence on this parameter is evident, clearly indicating by visual inspection that the curve for a value of 2.20 Å is much closer to experiment than those for 2.10 or 2.30 Å.

Figures 7 and 8 show the optimized calculations compared to the filtered data for all experimental geometries. The agreement ranges from good to excellent, with the exception of some portions of the [001] curve. As discussed above, much of the structure in this data set is strongly influenced by scattering at angles near a resonance in the Ni scattering amplitude. The results for this geometry are thus sensitive to the input scattering phase shifts and errors in the experimental geometry.

Plots of the r factor obtained by varying S-Ni₂ and d_1 for each geometry are given in Figs. 9 and 10, respectively. The results are summarized in Table III. There is very good consistency between the values obtained for each data curve, as well as good agreement with results of the Fourier-transform analysis presented previously. The final column in Table III gives the averaged values obtained from the results for each individual geometry. This analysis thus also indicates an expansion (11%) in the first Ni interplanar spacing. The exception to this consistent agreement is the value of the S-to-second-layer-Ni distance obtained from the 50° data, which indi-

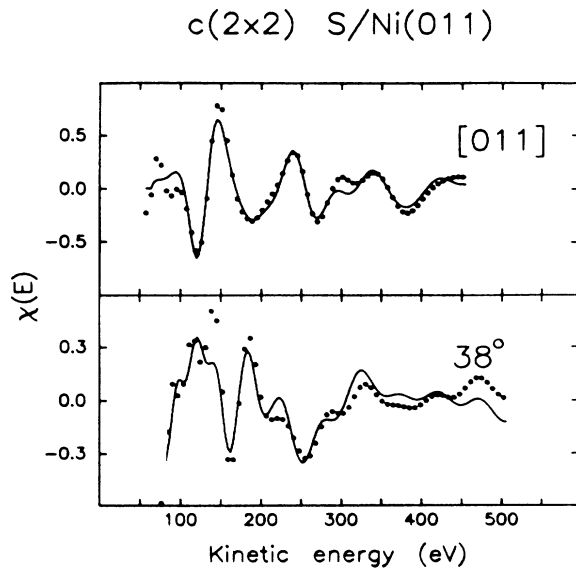


FIG. 7. Comparison of the filtered normal emission and 38° ARPEFS data (dotted lines) to multiple-scattering calculations (solid lines) for the best-fit geometry determined as described in the text.

cates a value 0.1 Å lower than the other values. This is outside the expected deviation based on the values obtained from the other curves. The value of S-Ni₂ for the 50° data was not included in the averaged value. A possible explanation for this discrepancy will be discussed below.

Having obtained very good agreement in the major structural parameters with the Fourier-transform results, we can now extend this *r*-factor analysis and try to obtain additional information. As indicated earlier, there is less intense structure in the Fourier transforms of the data, for which partial explanations have been offered. This structure provides a guide for testing the ARPEFS for further information. However, before proceeding to such an analysis, we will first comment briefly on the use of single-scattering versus multiple-scattering theories for this purpose.

Figure 11 contains a comparison of data taken at normal emission and at 50° with the optimized results ob-

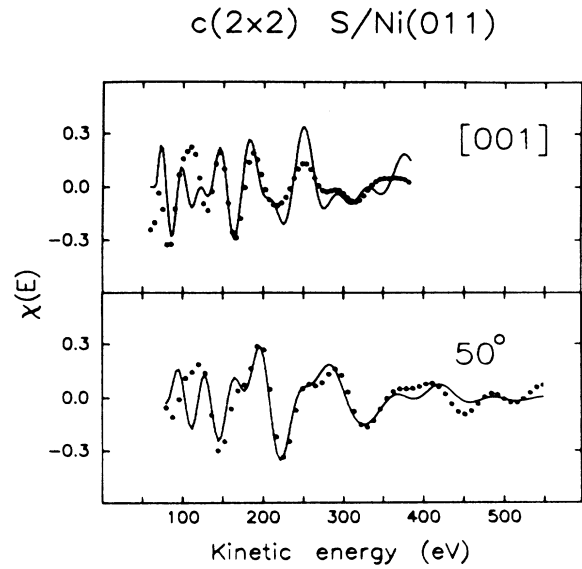


FIG. 8. Same as Fig. 7 for the [001] and 50° emission data.

tained for multiple-scattering (MS) and single-scattering (SS) theories. It is clear that the SS calculation provides good reproduction of the features in the experimental data for both geometries, though the quantitative agreement is better for the MS case. This is particularly true for the normal emission data. An *r*-factor analysis performing using SS calculations produces results that are similar to those obtained from the theory which includes the dominant multiple-scattering effects, but with shifts of 0.05 to 0.1 Å. The most pronounced example of this is illustrated in Fig. 12. This figure contains plots of the *r* factor obtained for variation of S-Ni₂ for the normal emission data, using single-scattering and multiple-scattering calculations. There is a shift of the SS minimum to a value indicating a S-to-second-layer-Ni bond length of 2.27 Å, 0.07 Å larger than the value obtained from the multiple-scattering analysis. This is, of course, another illustration of the effect of neglecting the double scattering phase shift discussed in Sec. IV A 1. In general, therefore, the parameters obtained from a SS analysis will vary by 0.05 to 0.1 Å with the experimental geometry, depending on whether or not there are important multiple-scattering

TABLE III. Structural parameters (in Å) obtained by comparison to multiple-scattering calculations for the four experimental geometries discussed in the text. S-Ni₂, *d*₁, and Δ (%) are the same parameters displayed in Table II, except as discussed in the text. The indicated errors represent the precision of the measurement and were determined from the values of χ² from the fit to theory and the curvature of the minimum for that particular parameter. The final column indicates the average of all geometries for *d*₁ and of the [011], 38°, and [001] results for S-Ni₂ and Δ (%).

Parameter	[011]	38°	50°	[001]	Avg.
S-Ni ₂	2.20(1)	2.19(1)	2.10(1)	2.21(1)	2.20(2)
<i>d</i> ₁	0.85(3)	0.81(1)	0.78(2)	0.81(2)	0.81(3)
Δ (%)	8	11		12	11(3)

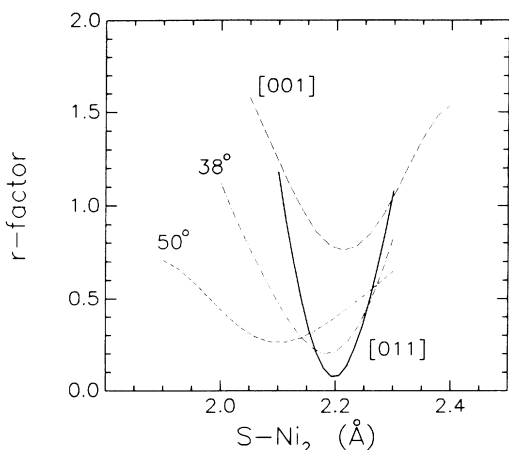


FIG. 9. Values of the r factor versus the S-to-second-layer-Ni (S-Ni₂) distance.

contributions—particularly additional forward-scattering events. The apparent values of nonstructural parameters which determine intensities, such as the electron mean-free path and σ_j^2 , will also appear to be dependent on the geometry, due to the forward-scattering enhancement discussed previously. Because the values given in Table III indicate that the precision (and most likely accuracy also) in the measurements is below the 0.1-Å level, and because we are interested in investigating the possibility of obtaining structural information on this scale, the inclusion of at least the dominant multiple-scattering effects is necessary. However, the simplicity of the SS calculations makes them very attractive for performing a preliminary analysis or for use in cases where possible errors on the order of 0.1 Å are not deemed important.

We now discuss the results of efforts to obtain additional structural information. In particular, we wish to con-

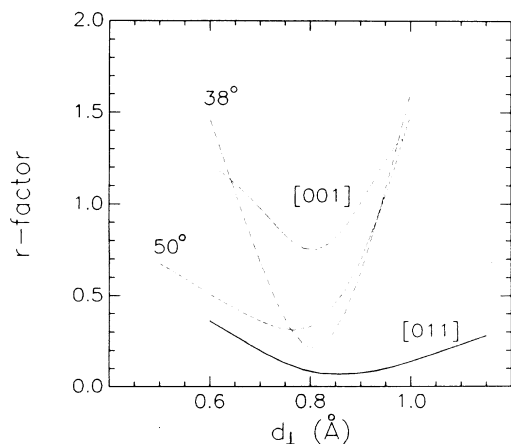


FIG. 10. Values of the r factor versus the distance of the S atom above the first Ni plane, d_1 .

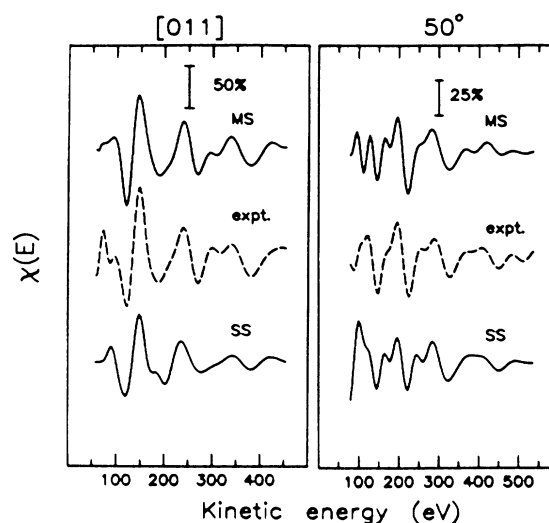


FIG. 11. Comparison of the results of multiple-scattering theory to single-scattering theory for the two experimental geometries indicated.

consider a possible explanation of the discrepancy noted previously in the value of S-Ni₂ distance obtained from the 50° data. The Fourier transform for this geometry exhibits a relatively strong feature at 8 Å which is due primarily to scattering from the second-layer Ni labeled (4) in Fig. 4. The photon polarization was directed within 12° of this atom and the scattering was very close to back-scattering. In contrast the second-layer Ni atom directly below the S atom lies in the nodal plane of the outgoing

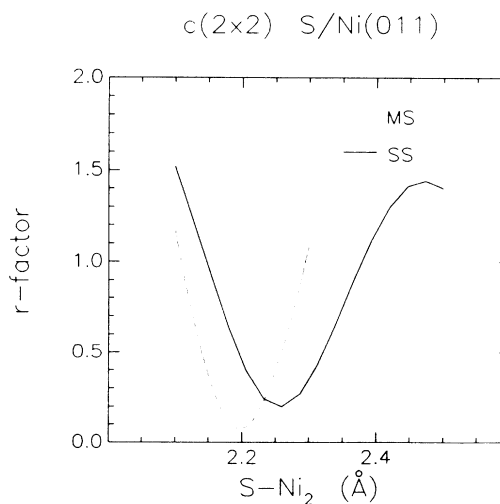


FIG. 12. Comparison of r factors obtained using a multiple-scattering theory to those obtained for a theory including only single scattering for the normal emission geometry versus S-Ni₂. The single-scattering theory indicates a minimum which is shifted by 0.07 Å.

photoelectron p wave. Thus, this geometry is sensitive to the distance to the second Ni layer as measured to the uncovered Ni atoms, whereas the normal emission case is very sensitive to the Ni atom directly below the S atom. The results presented in Table III thus suggest that Ni atoms in these two sites are inequivalent, with the uncovered Ni₂ atoms ~ 0.1 Å higher than the atopped Ni₂ atoms.

We have tested this explanation by performing additional calculations considering a buckled second layer. For the 50° data, a minimum in the r factor was found for a buckling which placed the uncovered Ni atoms 0.13 Å higher than the atopped Ni atoms, thus giving a value of the distance to the first Ni plane for the uncovered site which is essentially the same as a bulk interplanar separation. The 38° data also exhibited a lowered value of the minimum in the r factor for a buckling of 0.13 Å. The normal emission data showed very little sensitivity to the buckling, as would be expected since the photon polarization was directly nearly perpendicular to the surface, and the [001] data indicated a minimum for no buckling. Considering the much better fits obtained for the 38° and 50° data relative to the [001] data, for the reasons mentioned previously, we feel that these results support a buckled second-layer model.

The existence of a buckling of this nature is not difficult to accept. There is no *a priori* reason to expect the uncovered and atopped second-layer Ni atoms to assume equivalent positions. One might expect that the uncovered site would be closer in structure to the clean Ni surface, for which it is known that the first interplanar separation is contracted by 5–10% (Refs. 9 and 31) relative to the bulk, as compared to the expansion seen in the sulfur atopped site. This would lead to the uncovered second-layer Ni atoms assuming a position closer to the first Ni layer than the atopped atoms, as suggested by the data.

As a final case displaying the possibility of additional information, we consider the normal emission data. As indicated earlier, the peak at ~ 7.5 Å in the Fourier transform of the normal emission data has a large contribution due to scattering from four atoms in the third Ni layer. This suggests that the data for this geometry might provide some indication of the interplanar separation between the second and third Ni layers. Calculations were performed to test this hypothesis, and the results are presented in Fig. 13. These calculations were performed with a buckled second Ni layer as described above. The parameter, d_{23} , on the horizontal axis of Fig. 13, then represents the separation between the third-layer Ni atoms and the second-layer Ni atoms covered by S atoms. The r -factor values are given for two normal emission measurements and also for the 38° data. Both normal emission results indicate a broad minimum which is contracted from the bulk value. However, the deviation in the results obtained from the two measurements is approximately of the same magnitude as the apparent contraction. The 38° data indicate a value which is essentially the same as the bulk value. Note that the vertical scale for Fig. 13 is decreased by a factor of 2 relative to those in Figs. 9 and 10. Thus, the minima displayed for the varia-

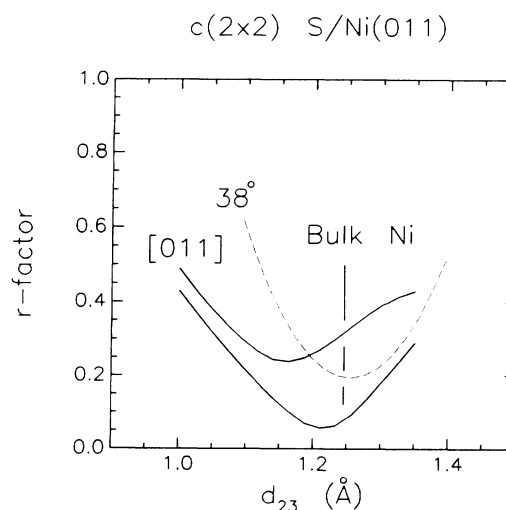


FIG. 13. Values of the r factor obtained for variation of the separation between the second and third Ni layers for two normal emission measurements and the 38° emission measurement.

tion of this parameter are very broad on the scale of most of the curves displayed in Figs. 9 and 10, and are more similar to the r -factor curve exhibited for variation of d_1 for the normal emission data in Fig. 10. The other two experimental geometries exhibited even less sensitivity to the variation of d_{23} , and thus are not given. The broad minima exhibited in this figure indicate that the changes produced by variation of this parameter are slight, and are thus susceptible to errors in the data and use of a rather simple r factor. On balance, however, a simple average of these results indicates a value of this separation which is contracted from the bulk value by $3 \pm 4\%$ (0.04 Å). This is based on a simple average of the results in Fig. 13 with equal weight for each measurement. This further means that the separation between the third-layer Ni atoms and the second-layer Ni atoms not covered by S atoms is expanded by $\sim 7\%$ due to the buckling. Continuing the analogy to the clean surface, this is to be compared with an expansion of 3–4% in the second- to third-layer separation determined for clean Ni on the basis of LEED and ion scattering data.³¹

V. HIGH COVERAGE RESULTS

We also studied the adsorption of S on Ni(011) for coverages above $\frac{1}{2}$ ML (monolayer). As S is adsorbed beyond the $c(2 \times 2)$ or $\frac{1}{2}$ ML point, distinct changes are observed in the LEED pattern. The $(\frac{1}{2}, \frac{1}{2})$ spots become elongated in the $[0\bar{1}1]$ direction, finally splitting to form a doublet. The separation between the two spots forming the doublet increases with increasing S coverage.

This behavior has been observed in several earlier studies and two explanations for the doubled $(\frac{1}{2}, \frac{1}{2})$ spots were proposed. Perdereau and Oudar³² suggested that continued S adsorption was accompanied by a homogeneous de-

crease of the S-S distance in the $[0\bar{1}1]$ direction. This results in a surface on which many of the S atoms are shifted from the rectangular hollow site determined for the $c(2 \times 2)$ structure toward a long-bridge site. One of the spots in the doublet observed in the LEED pattern is then explained by single scattering while the other is produced by multiple scattering.

The other, more plausible, model was presented by Mroz.³³ In his work, the doubling of the $(\frac{1}{2}, \frac{1}{2})$ spot was explained by considering the diffraction from a surface consisting of domains of N sulfur atoms separated by antiphase boundaries. By calculating the interference function for such a case, Mroz showed that the $(\frac{1}{2}, \frac{1}{2})$ spots would be split by an amount

$$d = 1/(2N - 1), \quad (9)$$

where d is measured relative to the distance between the integral order spots in the $[0\bar{1}1]$ direction. The coverage associated with a given splitting, or equivalently, a given domain size, is then determined by

$$\Theta_N = N/(2N - 1). \quad (10)$$

ARPEFS data obtained for a S/Ni(011) sample which exhibited a doubling of the $(\frac{1}{2}, \frac{1}{2})$ LEED spot is presented in Fig. 14. This sample was prepared in the same manner as the $c(2 \times 2)$ samples except that the H_2S exposure was continued until a doubling of the $(\frac{1}{2}, \frac{1}{2})$ spot was observed. This required ~ 5 L.

The lower curve in Fig. 14, curve (b), is the photoemission intensity as a function of the kinetic energy for the 38° $c(2 \times 2)$ data presented previously. The upper curve shows data obtained from the higher coverage sample. The curves are identical except for the increased total signal from the higher coverage surface, suggesting that the S remains in the rectangular hollow. Using the relative intensity change between the two curves and assuming a coverage of 0.5 ML for the $c(2 \times 2)$ case, we can estimate

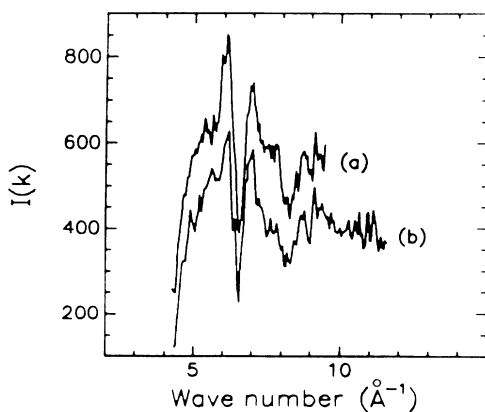


FIG. 14. Comparison of ARPEFS data taken with an emission direction of 38° for the $c(2 \times 2)$ $\frac{1}{2}$ ML surface (lower curve) to that obtained from a surface with an increased S coverage (upper curve).

a coverage of 0.65 ML for the higher coverage sample. With this increase in coverage of 30%, a model such as that proposed by Perdereau *et al.* would lead to much different ARPEFS due to the large number of S atoms which are shifted out of the rectangular hollow. Thus, these data rule out a homogeneous decrease of the S-S distance in the $[0\bar{1}1]$ direction as suggested by those authors.

We can estimate the domain size N by two methods. Using Eq. (9) and the value of d determined from the LEED pattern ($d=0.2 \pm 0.01$), we find $N \sim 3$. Alternatively, assuming a coverage of 0.5 for the $c(2 \times 2)$ surface and using the increase evident in Fig. 13, we can estimate a coverage of 0.65 ± 0.1 ML for the higher coverage surface. Employing Eq. (10), we then obtain $N \sim 2$. The higher coverage surface is thus determined to consist of antiphase domains approximately two to three sulfur atoms across in the $[0\bar{1}1]$ direction with the S adsorbed in the rectangular hollow site.

VI. CONCLUSIONS

We have presented a study of the surface structure of $c(2 \times 2)$ S/Ni(011) using an analysis of the angle-resolved-photoemission extended fine structure. The results obtained employing a Fourier-transform analysis and by comparisons to theoretical calculations are in good agreement, and also agree well the results of previous studies.⁷⁻⁹ Both methods of analysis enabled us to determine details of the surface structure such as the expansion of the first interplanar spacing reported by the ion scattering experiment,⁹ although the results of this experiment indicate a somewhat larger expansion than previously reported. Thus, the ARPEFS measurement indicates sulfur adsorption in a rectangular hollow site 2.20 ± 0.02 Å above a second-layer Ni atom and an expansion of (11%) in the first-to-second-Ni-layer distance. We have also suggested the possibility of a buckling of the second Ni layer on the basis of the r -factor analysis. Studies of this surface at higher sulfur coverage indicate that additional S is incorporated by the formation of antiphase domains in the $[0\bar{1}1]$ direction.

The good results obtained using the Fourier-transform analysis indicate the usefulness of this method. Consideration of possible adsorption sites should allow one to select experimental geometries which will serve to test these sites by highlighting backscattering from near neighbors. Examination of the Fourier-transformed data for two directions will almost certainly rule out several sites. The geometries selected for this experiment attempted to illustrate this point. It should also be noted that examination of the Fourier-transformed normal emission data alone provides strong evidence for the elimination of all sites except the rectangular hollow.

The possibility exists that for complicated systems, the structure will correspond to none of the sites that have been considered. Even so, examination of the Fourier transform can provide useful information. The excellent agreement obtained with relatively simple theories will then allow additional structures to be tested. The very different information which can be obtained for different

experimental geometries will also prove to be a great advantage.

We have also illustrated the effects of multiple scattering on the analysis of ARPEFS data. We have indicated that these effects cannot be ignored in quantitative interpretations. However, the dominant effects are easily understood qualitatively and do not alter dramatically the conceptual simplicity of the single-scattering model.

ACKNOWLEDGMENTS

This work was supported by the Director, Office of Energy Research, Office of Basic Energy Sciences, Chemical Sciences Division of the U.S. Department of Energy under Contract No. DE-AC03-76SF00098. It was performed at the Stanford Synchrotron Radiation Laboratory, which is supported by the U.S. Department of Energy's Office of Basic Energy Sciences.

*Permanent address: Department of Physics, Zhejiang University, Hangzhou, Zhejiang, China.

¹J. J. Barton, C. C. Bahr, Z. Hussain, S. W. Robey, J. G. Tobin, L. E. Klebanoff, and D. A. Shirley, *Phys. Rev. Lett.* **51**, 272 (1983).

²(a) S. Kono, C. S. Fadley, N. F. T. Hall, and Z. Hussain, *Phys. Rev. Lett.* **41**, 117 (1978); (b) S. Kono, S. M. Goldberg, N. F. T. Hall, and C. S. Fadley, *ibid.* **41**, 1831 (1978); (c) P. J. Orders, R. E. Connelly, N. F. T. Hall, and C. S. Fadley, *Phys. Rev. B* **24**, 6163 (1981).

³(a) S. D. Kevan, D. H. Rosenblatt, D. R. Denley, B.-C. Lu, and D. A. Shirley, *Phys. Rev. B* **20**, 4133 (1979); (b) S. D. Kevan, J. G. Tobin, D. H. Rosenblatt, R. F. Davis, and D. A. Shirley, *ibid.* **23**, 493 (1981); (c) S. D. Kevan, R. F. Davis, D. H. Rosenblatt, J. G. Tobin, M. G. Mason, D. A. Shirley, C. H. Li, and S. Y. Tong, *Phys. Rev. Lett.* **46**, 1629 (1981); (d) D. H. Rosenblatt, S. D. Kevan, J. G. Tobin, R. F. Davis, M. G. Mason, D. R. Denley, D. A. Shirley, Y. Huang, and S. Y. Tong, *Phys. Rev. B* **26**, 1812 (1982).

⁴D. H. Rosenblatt, J. G. Tobin, M. G. Mason, R. F. Davis, S. D. Kevan, D. A. Shirley, C. H. Li, and S. Y. Tong, *Phys. Rev. B* **23**, 3828 (1981).

⁵S. Y. Tong and C. H. Li, in *Chemistry and Physics of Solid Surfaces*, edited by R. Vanselow and W. England (CRC, Boca Raton, Fla., 1982), Vol. III, p. 287; C. H. Tong and S. Y. Tong, *Phys. Rev. Lett.* **43**, 526 (1979).

⁶P. J. Orders and C. S. Fadley, *Phys. Rev. B* **27**, 781 (1983); E. L. Bullock, C. S. Fadley, and P. J. Orders, *ibid.* **28**, 4867 (1983); M. Sagurton, E. L. Bullock, and C. S. Fadley, *ibid.* **30**, 7332 (1984).

⁷J. E. Demuth, D. W. Jepsen, and P. M. Marcus, *Phys. Rev. Lett.* **32**, 1182 (1974).

⁸P. M. Marcus, J. E. Demuth, and D. W. Jepsen, *Surf. Sci.* **53**, 501 (1973).

⁹J. F. van der Veen, R. M. Tromp, R. G. Smeeck, and F. W. Saris, *Surf. Sci.* **82**, 468 (1979).

¹⁰C. C. Bahr, J. J. Barton, Z. Hussain, S. W. Robey, J. G. Tobin, and D. A. Shirley, *Phys. Rev. B* (to be published).

¹¹J. J. Barton, S. W. Robey, C. C. Bahr, and S. A. Shirley, *First International Conference on the Structure of Surfaces, Berkeley, California*, Vol. 2 of *Springer Series in Surface Sciences*, edited by M. A. Van Hove and S. Y. Yung (Springer, New York, 1985).

¹²Z. Hussain, E. Umbach, D. A. Shirley, and J. Feldhaus, *Nucl. Instrum. Methods* **195**, 115 (1982).

¹³S. D. Kevan, Ph.D. thesis, University of California, Berkeley, 1980.

¹⁴30 vol. % glacial acetic acid, 30 vol. % nitric acid, 10 vol. %

sulfuric acid, 15 vol. % acetic acid.

¹⁵(a) J. J. Barton, C. C. Bahr, S. W. Robey, Z. Hussain, and D. A. Shirley, *Phys. Rev. B* **34**, 3807 (1986); (b) S. W. Robey, Ph.D. thesis, University of California, Berkeley, 1986 (unpublished).

¹⁶(a) A. Liebsch, *Phys. Rev. Lett.* **32**, 1203 (1974); (b) T. Fujikawa, *J. Electron Spectrosc. Relat. Phenom.* **26**, 79 (1982).

¹⁷P. A. Lee, *Phys. Rev. B* **12**, 5261 (1976).

¹⁸J. J. Barton, S. W. Robey, and D. A. Shirley, *Phys. Rev. B* **34**, 778 (1988).

¹⁹J. J. Barton and D. A. Shirley, *Phys. Rev. A* **32**, 1019 (1985); *Phys. Rev. B* **32**, 1892 (1985); **32**, 1906 (1985).

²⁰(a) P. A. Lee and J. B. Pendry, *Phys. Rev. B* **11**, 2795 (1975); (b) C. A. Ashely and S. Doniach, *ibid.* **11**, 1279 (1975); (c) P. A. Lee and G. Beni, *ibid.* **15**, 2862 (1977); (d) B. K. Teo, in *EXAFS Spectroscopy: Techniques and Applications*, edited by B. K. Teo and D. C. Joy (Plenum, New York, 1981), p. 22.

²¹J. J. Barton, Ph. D. thesis, University of California, Berkeley, 1985.

²²S. Y. Tong, M. A. Van Hove, and B. J. Mrstik, in *Proceeding of the Seventh International Vacuum Conference and the Third International Conference on Solid Surfaces, Vienna, 1977*, edited by R. Dobrozemsky *et al.* (IVC, ICSS, Vienna, 1977), Vol. 3, p. 2407.

²³Z. Hussain, D. A. Shirley, C. H. Li, and S. Y. Tong, *Proc. Natl. Acad. Sci. U.S.A.* **78**, 5293 (1981).

²⁴P. A. Lee, P. H. Citrin, P. Eisenberger, and B. M. Kincaid, *Rev. Mod. Phys.* **53**, 769 (1981).

²⁵M. P. Seah and W. A. Dench, *Surf. Interface Anal.* **1**, 1 (1979).

²⁶R. F. Wallis, B. C. Clark, R. Herman, and D. C. Grazis, *Phys. Rev.* **180**, 726 (1969); B. C. Clark, R. Herman, and R. F. Wallis, *ibid.* **139**, 860 (1965).

²⁷J. B. Pendry, *Low Energy Electron Diffraction* (Academic, London, 1974).

²⁸V. L. Moruzzi, J. F. Janak, and A. R. Williams, *Calculated Electronic Properties of Metals* (Pergamon, New York, 1978).

²⁹K. Schwarz, *Phys. Rev. B* **5**, 2466 (1972).

³⁰M. A. Van Hove and R. J. Koestner, in *Determination of Surface Structure by LEED*, edited by P. M. Marcus and F. Jona (Plenum, New York, 1984), p. 357.

³¹M. L. Xu and S. Y. Tong, *Phys. Rev. B* **31**, 6332 (1985); R. Feidenhans'l, J. E. Sorensen, and J. Stensgaard, *Surf. Sci.* **134**, 329 (1983).

³²M. Perdereau and J. Oudar, *Surf. Sci.* **20**, 80 (1970).

³³S. Mroz, *Surf. Sci.* **83**, L625 (1979).